# Hybrid Control for Improved Pressure and Flow Tracking in Mechanical Ventilation

Lars van de Kamp, Isabelle Franklin, Bas van Loon, Nathan van de Wouw, *Fellow, IEEE*, and Tom Oomen, *Senior Member, IEEE*

***Abstract*—Mechanical ventilators are essential for patients who are unable to breathe independently. The aim of this article is to develop a systematic control design methodology that achieves accurate tracking of both the pressure and flow to ensure comfortable breathing for the patient. A hybrid controller is introduced that ensures improved baseflow tracking performance. The actual controller design leverages frequency-based techniques and is based on static decoupling and the factorized Nyquist criterion. Furthermore, a theoretical stability analysis of the hybrid controller is presented. The presented control strategy is implemented in a real ventilator, and it is demonstrated that the tracking performance is improved by conducting an experimental case study.**

***Index Terms*—Hybrid control system, mechanical ventilation, mechatronics, static decoupling.**

## I. Introduction

MECHANICAL ventilation is crucial in intensive care units (ICUs) to assist patients unable to breathe independently. The goal of mechanical ventilation is to ensure adequate oxygenation and carbon dioxide elimination for a large variety of patients [1]. In 2005 alone, over 790 000 patients were reliant on mechanical ventilation to survive [2]. Therefore, improving mechanical ventilation improves treatment for a large population worldwide, especially during the flu season or a worldwide pandemic, such as the COVID-19 pandemic in recent years.

In pressure-controlled ventilation, the ventilator aims to track a pressure profile at the patient's airway to ensure sufficient airflow in and out of the lungs [3]. In addition, the ventilator aims to track a baseflow target, which is a constant flow target that ensures that the breathing hoses contain fresh air, i.e., residues of $CO_2$-rich exhaled air are washed out. A schematic representation of the system, including breathing hose and patient, is depicted in Fig. 1. From a control perspective, the system tracks two References, i.e., the pressure target and the baseflow target. The measured output that should track these references are the output pressure ($p_{\text{out}}$), output flow ($Q_{\text{out}}$), and expiration flow ($Q_{\text{exp}}$).[1] During an inspiration, a part of the output flow is used to build up pressure in the lungs, and a part is used as a baseflow to flush the hose. There are two actuators to be controlled, i.e., a blower and an expiration valve. A change in the actuator signal for either the blower and/or the expiration valve results in a change in both the pressure and flow outputs. Inherently, these multiple inputs and outputs are dynamically coupled. Ignoring this coupling during control design leads to performance limitations and stability issues. Therefore, such coupling must be taken into account during controller design.

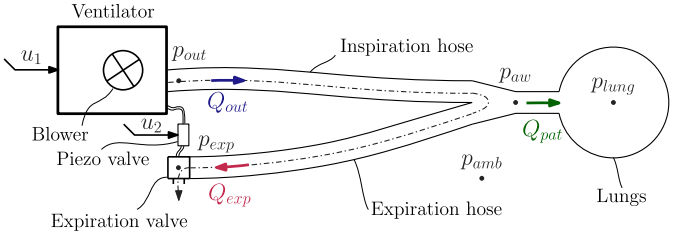


Fig. 1. Schematic overview of the ventilator and patient system, with the definition of the important pressures and flows. The inputs $u_1$ and $u_2$ of the system are, respectively, the blower revolution speed and the piezo voltage.

Another controller design challenge is the switch between two flow sensors to track the baseflow target during a full breathing cycle. In Fig. 2, an example of the reference trajectories for the airway pressure and baseflow is depicted together with the exemplary response of the associated pressure and flow signals. In this figure, it is clear that the output flow ($Q_{\text{out}}$) cannot track the baseflow reference during the whole breathing cycle; namely, during an inspiration, typically more output flow is required than the baseflow target in order to pressurize the lungs. Similarly, the expiration flow ($Q_{\text{exp}}$) cannot be used to track the baseflow during expiration because of the extra air

Received 23 May 2025; revised 28 May 2025 and 8 October 2025; accepted 20 January 2026. Date of publication 27 February 2026; date of current version 5 May 2026. This work was supported by the Demcon Life Sciences and Health, Best. Recommended by Associate Editor M. Ruderman. *(Corresponding author: Lars van de Kamp.)*

Lars van de Kamp is with the Dynamics and Control Section, Department of Mechanical Engineering, Eindhoven University of Technology, 5600 MB Eindhoven, The Netherlands, and also with the Demcon Life Sciences and Health, 5683 CR Best, The Netherlands (e-mail: l.g.j.v.d.kamp@tue.nl).

Isabelle Franklin and Bas van Loon are with the Demcon Life Sciences and Health, 5683 CR Best, The Netherlands (e-mail: isabelle.franklin@demcon.com; bas.van.loon@demcon.com).

Nathan van de Wouw is with the Dynamics and Control Section, Department of Mechanical Engineering, Eindhoven University of Technology, 5600 MB Eindhoven, The Netherlands (e-mail: N.v.d.wouw@tue.nl).

Tom Oomen is with the Control Systems Technology Section, Department of Mechanical Engineering, Eindhoven University of Technology, 5600 MB Eindhoven, The Netherlands, and also with Delft Center for Systems and Control, Delft University of Technology, 2628 CD Delft, The Netherlands (e-mail: t.a.e.Oomen@tue.nl).

Digital Object Identifier 10.1109/TCST.2026.3661100

[1] A detailed explanation of how these three outputs should track the two references is provided in Section II.

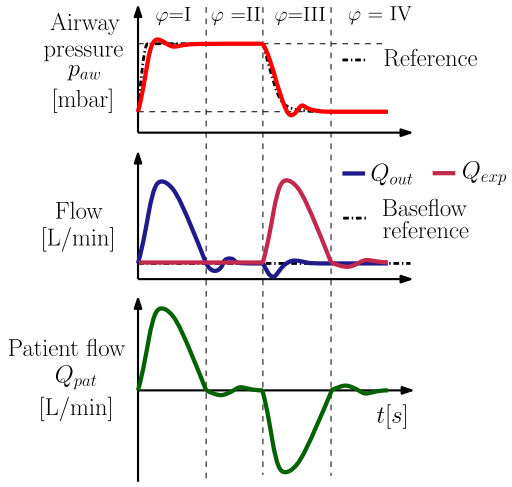


Fig. 2. Schematic overview of mechanically delivered breath, with the definition of the references and the measured pressure and flows. The locations of the pressure and flows within the system are indicated in Fig. 1.

the patient exhales. As a result, a switch between the output flow $Q_{\text{out}}$ and expiration flow $Q_{\text{exp}}$ is necessary to define the baseflow during a full breathing cycle.

Accurate tracking of the pressure and flow references ensures sufficient fresh air delivery and improves patient comfort. Improved pressure tracking can decrease the incidence of patient–ventilator asynchrony [4]. This is important because patient–ventilator asynchrony is associated with longer hospital stays and increased mortality rates [5]. Furthermore, accurate pressure and flow tracking for a wide range of patients improves consistency of treatment over these different patients.

The controller design must satisfy the following requirements.

1) The controller must simultaneously track the pressure and the baseflow references while accounting for multivariate input–output interaction.
2) The controller must employ a sensor-switching strategy to ensure accurate baseflow tracking across all phases of the breathing cycle by appropriately selecting different flow sensors.

From a control perspective, the unknown patient is part of the to-be-controlled system. The challenging problem of pressure and flow tracking in the presence of widely varying patients has accelerated the development of a wide range of pressure control methodologies. Methods that resulted in improved tracking performance of either pressure or flow targets are variable-gain control [4], adaptive feedback control [6], model predictive control [7], and adaptive hose compensation control [8]. The tracking performance can be even further improved by leveraging the repetitive nature of breathing with iterative learning control [9], [10] and repetitive control [11], [12].

Although the above control techniques have substantially improved the pressure tracking performance, they do not yet satisfy both requirements 1) and 2) above. The challenge of simultaneously tracking the pressure and the flow via the blower and the expiration valve has not been addressed in the literature. In the literature on multivariable control, there are different solutions to cope with interaction during control design [13]. In this article, the focus lies on decoupling control [14] as it is an intuitive approach to deal with interaction in the system dynamics, requirement 1). Decoupling control helps to reduce interaction (i.e., diagonalize the system's input–output dynamics), which potentially makes it possible to design controllers for the pressure and flow loops separately. In addition, a switch is required to track the flow target for an entire breath, requirement 2); also, this problem has not been addressed in the literature.

The main contribution of this article is to present an intuitive design procedure for a hybrid (switching), multivariable control strategy for mechanical ventilation that is able to cope with interaction to improve the tracking performance. The first contribution is an interaction analysis of the MIMO ventilation system. The second contribution is the design and implementation of a novel controller in an experimental setup that is robust for a wide variety of patients. The third contribution is a dedicated stability proof for the presented hybrid control system. Preliminary results of this article appear in [15]. Main extensions compared to [15] include a robustness analysis for a wide variety of patients and a formal stability proof of the hybrid controller presented in this article.

This article follows the following structure. In Section II, the ventilation system, the control goals and challenges, and the envisioned approach are presented. In Section III, the control design procedure is presented in detail. In Section IV, the control design procedure is followed for an experimental mechanical ventilation setup. Results of the interaction analysis, the decoupling procedure, and the control design approach are shown. Thereafter, in Section V, a performance analysis is conducted based on a set of emulated patients in the experimental setup. Finally, in Section VI, conclusions and recommendations are given.

*Notations:* A continuous function $\gamma : \mathbb{R}_{\geq 0} \to \mathbb{R}_{\geq 0}$ is of class $\mathcal{K}$($\gamma \in \mathcal{K}$) if it is strictly increasing, and $\gamma(0) = 0$. If, in addition, $\gamma(r) \to \infty$ as $r \to \infty$, then $\gamma$ is of class $\mathcal{K}_\infty$ ($\gamma \in \mathcal{K}_\infty$). A continuous function $\beta : \mathbb{R}_{\geq 0} \times \mathbb{R}_{\geq 0} \to \mathbb{R}_{\geq 0}$ is of class $\mathcal{KL}$ ($\beta \in \mathcal{KL}$) if, for each fixed $t$, $\beta(\cdot, t) \in \mathcal{K}$, and, for each fixed $s$, $\beta(s, \cdot)$ is decreasing and $\beta(s, t) \to 0$ as $t \to \infty$.

## II. Control Problem Formulation

In this section, the control problem formulation is presented. In Section II-A, the mechanical ventilation system is described from a control perspective. Thereafter, the control goals and challenges are described in Section II-B. Last, the control approach is presented in Section II-C.

### A. High-Level System Description

Considering Fig. 1, the main components of this system are the blower, the inspiration and expiration hose, the expiration valve, the piezo actuator, and the patient. A patient is characterized by the lung resistance and compliance, which influence the pressures and flows in the rest of the system. The blower and the expiration valve should jointly ensure the pressure build-up at the outlet of the blower, i.e., $p_{\text{out}}$, which is realized by a combination of increasing the blower speed

$u_1$ and by increasing the Piezo voltage $u_2$, i.e., closing of the expiration valve. Using a model of the breathing hose, we can control $p_{\text{out}}$ in order to achieve the desired patient airway pressure $p_{\text{aw}}$ defined by the clinician.

A mechanical breath can typically be subdivided into four breath phases ($\varphi$), as shown in Fig. 2. The inspiration consists of phases $\varphi \in \{\text{I, II}\}$, where the airway pressure is high, and the expiration is covered by phases $\varphi \in \{\text{III, IV}\}$, where the airway pressure is low. A flow $Q_{\text{out}}$ in the inspiration hose is caused by the pressure difference between the outlet pressure $p_{\text{out}}$ and the airway pressure $p_{\text{aw}}$ of the patient. The pressure difference between the airway and lung ($p_{\text{aw}}$ and $p_{\text{lung}}$) induces the patient flow $Q_{\text{pat}}$, while the difference between the airway pressure and pressure located near the expiration valve ($p_{\text{exp}}$) induces an expiration flow $Q_{\text{exp}}$ through the expiration hose. During all phases of the breath, a baseflow $Q_{\text{bf}}$ must be present from the output of the ventilator straight to the expiration valve to refresh the air in the hoses. The baseflow measurement (i.e., the variable $Q_{\text{bf}}$ that should track the baseflow reference) cannot be expressed by only one measured flow variable during the whole breathing cycle but needs to be reconstructed using both the outlet and expiration flow. Therefore, the baseflow $Q_{\text{bf}}$ is defined as follows:

$$Q_{\text{bf}} := \begin{cases} Q_{\text{exp}} \text{ if } \varphi \in \{\text{I, II}\} \\ Q_{\text{out}} \text{ if } \varphi \in \{\text{III, IV}\}. \end{cases} \tag{1}$$

### B. Control Goals and Challenges

This article considers pressure-controlled mandatory ventilation (PCMV) of fully sedated patients. The goal of this system in PCMV mode is to track a preset airway pressure reference $p_{\text{aw,target}}$ given by the clinician while maintaining a constant level of baseflow $Q_{\text{bf,target}}$ during the entire breath; see the dash-dotted lines in Fig. 2. The overall control goal is to minimize the tracking errors, defined by

$$\begin{aligned} e_p &:= p_{\text{out}} - p_{\text{out,target}} \\ e_Q &:= Q_{\text{bf}} - Q_{\text{bf,target}} \end{aligned} \tag{2}$$

where $p_{\text{out,target}}$ is derived from the airway pressure reference $p_{\text{aw,target}}$ based on model of a hose, as described in [8]. In a clinical context, a sensor can only be used for either control or monitoring purposes, and $p_{\text{aw}}$ is used for monitoring purposes only. Therefore, the control goal is defined on the outlet pressure level since the outlet pressure $p_{\text{out}}$ is a measured system output. Furthermore, the measured flow variables, the outlet flow $Q_{\text{out}}$ and expiration flow $Q_{\text{exp}}$, are both used in the definition of the baseflow $Q_{\text{bf}}$ in (1). This induces a switch in the measured output used for feedback and, hence, introduces a switch in the control system and closed-loop dynamics, which challenges the controller design. Closed-loop stability must be guaranteed under switching by design of a systematic and user-friendly controller. A systematic approach makes controller maintenance for engineers easier in practice.

Besides the challenge related to the switching flow error, see (1) and (2), also the inherent coupling of the multivariable inputs and outputs through the system dynamics challenges the controller design. This coupling requires a control design that copes with such multivariable interaction. If it is not taken into account in the design process, this interaction can result in an unstable system or poor performance. Therefore, the last control goal is to design a decentralized controller that is robust for interaction. This control approach is user-friendly because it does not require an iterative technique to ensure closed-loop stability.

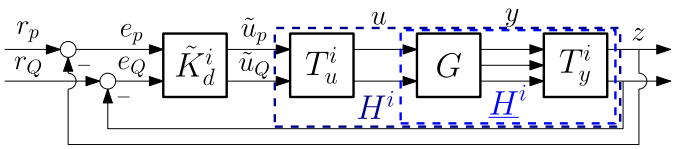


Fig. 3. Schematic overview of the proposed control scheme with $i \in \{1, 2\}$. During inspiration (phases $\varphi \in \{\text{I, II}\}$), $i = 1$, and during (phases $\varphi \in \{\text{III, IV}\}$), expiration $i = 2$.

### C. Control Approach

In this section, a high-level explanation of the main contribution is presented. Consider Fig. 3, there are two inputs, i.e., $u = [u_1,\ u_2]^\top$, where $u_1$ is the blower speed and $u_2$ is the piezo voltage. The plant has three measured outputs, $y = [y_1,\ y_2,\ y_3]^\top$, which represent $p_{\text{out}}$, $Q_{\text{out}}$, and $Q_{\text{exp}}$, respectively. The output selection matrix $T_y^i$ selects the appropriate system outputs during each breathing phase such that the performance variables are defined as

$$z := \begin{bmatrix} p_{\text{out}} \\ Q_{\text{bf}} \end{bmatrix} = \begin{cases} T_y^1 y = \begin{bmatrix} 1 & 0 & 0 \\ 0 & 0 & 1 \end{bmatrix} y & \text{if } \varphi \in \{\text{I, II}\} \\ T_y^2 y = \begin{bmatrix} 1 & 0 & 0 \\ 0 & 1 & 0 \end{bmatrix} y & \text{if } \varphi \in \{\text{III, IV}\}. \end{cases} \tag{3}$$

Hence, we have a $2 \times 2$ MIMO system in which switches occur at the transitions of breathing phases (between $\varphi = \text{II}$ and $\varphi = \text{III}$ and between $\varphi = \text{IV}$ and $\varphi = \text{I}$) at repetitive, exactly known, moments in time (defined by the pressure reference).

Designing a decentralized controller $\tilde{K}_d^i$ and a decoupling matrix $T_u^i$ is possible after identification of the plant dynamics $G$. In Section III, our control design procedure is presented, and each step is explained in detail.

## III. Controller Design Procedure

In this section, the controller design procedure is presented. To satisfy requirements 1) and 2), an approach inspired by the advanced motion control procedure in [14] is extended to address the switching between the different flow sensors. The design approach consists of the following steps.

1) Identify the plant $G$ using frequency response function (FRF) measurements, and define the systems $\underline{H}^i := T_y^i G$ where $T_y^i$ is the output selection matrix for $i = 1, 2$ [recall that $i = 1$ for $\varphi \in \{\text{I, II}\}$ and $i = 2$ for $\varphi \in \{\text{III, IV}\}$; see (3)]. The outputs of $\underline{H}^i$ remain physically interpretable.
2) Analyze the interaction of $\underline{H}^i$ using the relative gain array (RGA) $\Lambda^i$ for $i = 1, 2$ (see definition in Section III-A).

a) If the system is coupled, go to step 3).
b) If the system is decoupled, define $T_u^i = I_{2\times 2}$ and $H^i := T_y^i G T_u^i$ for $i = 1, 2$, and go to step 4).

3) Design of the static decoupling matrices $T_u^i$, for $i = 1, 2$, using the interaction index $\phi^i$ (see definition in Section III-A) to reduce interaction below the bandwidth of the system and define the systems $H^i := T_y^i G T_u^i$ for $i = 1, 2$. The inputs of $H^i$ are in the transformed domain, while the outputs remain physically interpretable.
4) Design of stabilizing decentralized controllers $\tilde{K}_d^i$, with $i = 1, 2$, using standard loop-shaping techniques.
   a) If there are residual interactions after the static decoupling step, then use the factorized Nyquist criterion to ensure robustness for such residual interactions.
5) Analyze the stability of the switched closed-loop system.

The control design methodology for the individual systems in this work is entirely based on frequency-domain data of the dynamics. This approach offers several advantages: it enables robust decoupling and intuitive loop-shaping of single-input–single-output loops through straightforward stability and robustness analysis using tools such as Nyquist plots and provides clear visual feedback for engineers in the design process. Frequency-based techniques are also widely adopted in industry due to their transparency and ease of use for controller tuning. In contrast, state-space models, while powerful for theoretical analysis (e.g., stability), often require detailed internal knowledge of the system and are computationally intensive to obtain.

In our methodology, Steps 1–4 (system identification, interaction analysis, static decoupling, and decentralized controller design) are performed exclusively in the frequency domain, without relying on state-space models. This ensures that the controller design is easy to apply in practice, leveraging only measured frequency response data. Note that steps 1)–4) should be executed for both the inspiration and expiration phases (i.e., for $i = 1$ during inspiration and for $i = 2$ during expiration).

However, for the stability analysis of the overall switched (hybrid) system in Step 5, a state-space representation becomes essential. Namely, there is currently no frequency-domain method available for rigorously proving the stability of switched linear systems of this form. Therefore, we employ a state-space model solely for the purpose of establishing input-to-state stability of the closed-loop system under switching.

This clear separation between frequency-based techniques for controller design and state-space models for stability proof ensures both practical applicability and theoretical rigor in our approach. In the next sections, steps 2)–5) are explained in more detail, in Sections III-A–III-D, respectively.

### A. Interaction Analysis (Step 2)

A frequency-domain interpretation of interaction, the RGA [16], is used for the two-sided interaction analysis. Considering a system represented by the FRF $\underline{H}^i = T_y^i G$ (see Fig. 3), then the RGA [13] is defined as

$$\Lambda^i(j\omega) := \underline{H}^i(j\omega) \odot \left(\underline{H}^i(j\omega)^{-1}\right)^\top, \quad \omega \in \mathbb{R}, \quad i \in \{1, 2\} \tag{4}$$

where $\odot$ denotes the elementwise product. For a $2 \times 2$ system, the RGA is fully determined by the interaction index $\phi$ as follows:

$$\Lambda^i(j\omega) = \begin{bmatrix} \frac{1}{1-\phi^i(j\omega)} & \frac{-\phi^i(j\omega)}{1-\phi^i(j\omega)} \\ \frac{-\phi^i(j\omega)}{1-\phi^i(j\omega)} & \frac{1}{1-\phi^i(j\omega)} \end{bmatrix} \tag{5}$$

with

$$\phi^i(j\omega) := \frac{\underline{H}^{i,12}(j\omega)\underline{H}^{i,21}(j\omega)}{\underline{H}^{i,11}(j\omega)\underline{H}^{i,22}(j\omega)}, \quad \omega \in \mathbb{R}, \quad i \in \{1, 2\} \tag{6}$$

where $\underline{H}^{i,vw}$, with $v, w \in \{1, 2\}$, denotes the $\{v, w\}$ elements of $\underline{H}^i$. An interaction index of zero means that no interaction is present, which allows for decentralized controller design.

### B. Design of the Static Decoupling Matrix (Step 3)

The interaction within a system can be reduced by decoupling the system dynamics. In mechanical ventilation, obtaining accurate plant models is challenging due to the unknown variability in patient dynamics. This variability complicates dynamic decoupling, as each plant (involving different patients) exhibits slight differences, resulting in a range of FRFs. However, static decoupling remains feasible because the patient dynamics only slightly affect the static behavior, which allows for robust performance design of a static decoupling matrix.

In static decoupling, a constant matrix $T_u^i$ computes a linear transformation of the control output of $\tilde{K}_d^i$ (see Fig. 3). These transformed controller outputs are subsequently used as plant inputs to reduce interaction by diagonalizing the plant. While plant data are typically complex-valued due to frequency response characteristics, the decoupling matrix must be real-valued to enable implementation, as actuators only allow real input values. A real-valued inverse of the frequency response data can be approximated using the ALIGN algorithm [13], leading to a static decoupling matrix

$$T_u^i := \text{ALIGN}\left(\bar{\underline{H}}^i\right) \quad \forall i \in \{1, 2\} \tag{7}$$

where $\bar{\underline{H}}^i$ is the average frequency response data over a certain (low) frequency range where the slope of the Bode plots is zero.

### C. Decentralized Controller Design (Step 4)

Design of the decentralized controllers in the frequency domain is done using traditional loop-shaping methods, and stability of the associated closed-loop systems is analyzed using the Nyquist criterion (see [13] for details).

The systematic controller design approach in the frequency domain must provide a clear guide on how to cope with residual interaction since the static decoupling does typically not fully remove interaction in the entire frequency range of interest. The factorized Nyquist criterion satisfies this requirement and helps to design controllers that are robust against interaction by taking the interaction into account during the design process. The factorized Nyquist criterion used for decentralized design is briefly described below (see also [17]).

Consider the system $H^i(j\omega) := T_y^i G(j\omega) T_u^i \in \mathbb{C}^{2\times 2}$ with the diagonal terms

$$\tilde{H}^i(j\omega) = \operatorname{diag}\left(H^{i,vv}(j\omega)\right) \tag{8}$$

with $v = 1, 2$ and the normalized off-diagonal terms

$$E^i(j\omega) = \left(H^i(j\omega) - \tilde{H}^i(j\omega)\right)\left(\tilde{H}^i\right)^{-1}(j\omega) \tag{9}$$

with $E^i \in \mathbb{C}^{2\times 2}$, $i \in \{1, 2\}$. For the remainder of this derivation, the notation is simplified for readability. Therefore, we omit the superscript $i$ and $(j\omega)$. The return difference matrix is defined as

$$I + H\tilde{K}_d = I + (I + E)\tilde{H}\tilde{K}_d = \left(I + E\tilde{\mathcal{T}}\right)\left(I + \tilde{H}\tilde{K}_d\right) \tag{10}$$

with $I \in \mathbb{R}^{2\times 2}$ the identity matrix, decentralized controller $\tilde{K}_d \in \mathbb{C}^{2\times 2}$, and

$$\tilde{\mathcal{T}} = \tilde{H}\tilde{K}_d\left(I + \tilde{H}\tilde{K}_d\right)^{-1}. \tag{11}$$

$\tilde{T} \in \mathbb{C}^{2\times 2}$, which is the complementary sensitivity that would be obtained if the system were diagonal, i.e., interaction-free. This results in the sensitivity function (including interaction)

$$\left(I + H\tilde{K}_d\right)^{-1} = \underbrace{\left(I + \tilde{H}\tilde{K}_d\right)^{-1}}_{\tilde{S}}\underbrace{\left(I + E\tilde{\mathcal{T}}\right)^{-1}}_{\text{interaction}} \tag{12}$$

with $\tilde{S} \in \mathbb{C}^{2\times 2}$ being the sensitivity of the diagonal terms. For the MIMO system to be stable, $\tilde{S}$ and the interaction term in (12) must both be stable.

The first term $\tilde{S}$ is stable by designing a strictly proper controller that does not contain any unstable pole–zero cancellations, while a criterion for the interaction term to be stable can be derived based on the small-gain theorem [18]. Note that the interaction term consists of a part $(E)$ that only depends on the plant and a part $(\tilde{\mathcal{T}})$ that consists of the diagonalized plant and controller. The interaction term is stable if

$$\rho\left(E(j\omega)\tilde{\mathcal{T}}(j\omega)\right) < 1 \quad \forall\omega \tag{13}$$

where $\rho$ denotes the spectral radius. Furthermore, it holds that

$$\rho\left(E\tilde{\mathcal{T}}\right) \le \mu_{\tilde{\mathcal{T}}}\left(E\tilde{\mathcal{T}}\right) \le \bar{\sigma}\left(\tilde{\mathcal{T}}\right)\mu_{\tilde{\mathcal{T}}}(E) \tag{14}$$

in which $(j\omega)$ is omitted for clarity and where $\bar{\sigma}(\tilde{\mathcal{T}})$ is the maximum singular value of $\tilde{\mathcal{T}}$ and $\mu_{\tilde{\mathcal{T}}}(E)$ is the structured singular value of $E$ with respect to the structure of $\tilde{\mathcal{T}}$, which is diagonal. Using (13) and (14), we conclude that the controller is robust against interaction, and the resulting closed-loop system is stable if

$$\bar{\sigma}\left(\tilde{\mathcal{T}}(j\omega)\right) < \mu_{\tilde{\mathcal{T}}}^{-1}\left(E(j\omega)\right) \quad \forall\omega. \tag{15}$$

This frequency-dependent criterion is used as a design tool for each of the two SISO controllers $\tilde{K}_d^1$ and $\tilde{K}_d^2$ to be robust against interaction.

Switching between the controllers and static decoupling matrices, induced by the switch in the output selection matrices [see (3)], requires an additional stability analysis based on hybrid system theory.

### D. Switching Closed-Loop System Dynamics and Stability Analysis

In this section, a state-space representation of the switched system dynamics is given. In addition, (input-to-state) stability of the switched system is proven.

The state-space representation of the plant dynamics $G$, shown in Fig. 3, is given by

$$\begin{aligned} \dot{x}_G &= A_G x_G + B_G u \\ y &= C_G x_G + D_G u \end{aligned} \tag{16}$$

where $x_G \in \mathbb{R}^{n_G}$ with $n_G > 0$ is the plant state. Let $A_G \in \mathbb{R}^{n_G \times n_G}$, $B_G \in \mathbb{R}^{n_G\times 2}$, $C_G \in \mathbb{R}^{3\times n_G}$, and $D_G \in \mathbb{R}^{3\times 2}$ be the system matrices. Note that switching does not occur within the plant dynamics. Next, the decoupling matrices $T_u^i$ and the sensor selection matrices $T_y^i$ (see Fig. 3) are defined: in the scope of the control structure of Fig. 3, the following static decoupling matrices and the output selection matrices are defined:

$$T_u^1 = \begin{bmatrix} T_{u_{11}}^1 & T_{u_{12}}^1 \\ T_{u_{21}}^1 & T_{u_{22}}^1 \end{bmatrix}, \text{and } T_y^1 = \begin{bmatrix} 1 & 0 & 0 \\ 0 & 0 & 1 \end{bmatrix} \tag{17}$$

and

$$T_u^2 = \begin{bmatrix} T_{u_{11}}^2 & T_{u_{12}}^2 \\ T_{u_{21}}^2 & T_{u_{22}}^2 \end{bmatrix}, \text{and } T_y^2 = \begin{bmatrix} 1 & 0 & 0 \\ 0 & 1 & 0 \end{bmatrix}. \tag{18}$$

Note that the output selection matrices represent switching in the sensor set used for feedback, and the decoupling matrices are switches in accordance to warrant decoupling. Last, the switching controller is defined as

$$\begin{aligned} \dot{x}_c &= A_c^i x_c + B_c^i e \\ \tilde{u} &= C_c^i x_c + D_c^i e \end{aligned} \tag{19}$$

where $e = [e_p, e_Q]^\top \in \mathbb{R}^2$ is the tracking error and $x_c \in \mathbb{R}^{n_c}$ are the internal controller states with $n_c$ being the number of states. Let $A_c^i \in \mathbb{R}^{n_c\times n_c}$, $B_c^i \in \mathbb{R}^{n_c\times 2}$, $C_c^i \in \mathbb{R}^{2\times n_c}$, and $D_c^i \in \mathbb{R}^{2\times 2}$ be the system matrices. Switching, in the controller, the output selection matrix, and the decoupling matrix, occurs via the following time-based switching law:

$$i(t) = \begin{cases} 1, & \text{for } t \in \left[k\left(T_{\text{exp}} + T_{\text{insp}}\right), \right. \\ & \left. \quad k\left(T_{\text{exp}} + T_{\text{insp}}\right) + T_{\text{insp}}\right) \\ 2, & \text{for } t \in \left[k\left(T_{\text{exp}} + T_{\text{insp}}\right) + T_{\text{insp}}, \right. \\ & \left. \quad (k+1)\left(T_{\text{exp}} + T_{\text{insp}}\right)\right) \end{cases} \tag{20}$$

for $k = 0, 1, 2, \ldots$, and where $T_{\text{insp}}$ and $T_{\text{exp}}$ are the inspiration and expiration time, respectively. This switching rules exhibits a switch whenever the breathing phase $\varphi$ changes from $\varphi = \text{II}$ to $\varphi = \text{III}$ and from $\varphi = \text{IV}$ to $\varphi = \text{I}$, which are fixed in time; see Fig. 2.

Let $x = [x_G, x_c]^\top \in \mathbb{R}^{n_p}$, with $n_p = n_G + n_c$, be the extended state space, the dynamics of which is governed by [combining (16)–(20)]

$$\begin{aligned} \dot{x} &= \begin{bmatrix} A_G & B_G T_u^i C_c^i \\ 0 & A_c^i \end{bmatrix} x + \begin{bmatrix} B_G T_u^i D_c^i \\ B_c^i \end{bmatrix} e \\ y &= \begin{bmatrix} C_G & D_G T_u^i C_c^i \end{bmatrix} x + D_G T_u^i D_c^i e \end{aligned} \tag{21}$$

with $i \in \{1,2\}$. The closed-loop dynamics are obtained by finding an expression for the tracking error $e = r - T_y^i y$ as a function of $x$ and $r$ and substituting it into (21), which results in the switched closed-loop system

$$\dot{x} = \underbrace{\left( \begin{bmatrix} A_G & B_G T_u^i C_c^i \\ 0 & A_c^i \end{bmatrix} - \begin{bmatrix} B_G T_u^i D_c^i \\ B_c^i \end{bmatrix} \mathrm{MT}_y^i \begin{bmatrix} C_G \\ D_G T_u^i C_c^i \end{bmatrix}^\top \right)}_{A_{\mathrm{cl}}^i} x + \underbrace{\begin{bmatrix} B_G T_u^i D_c^i \\ B_c^i \end{bmatrix}}_{B_{\mathrm{cl}}^i} M r \tag{22}$$

with

$$M := \left( I + T_y^i D_G T_u^i D_c^i \right)^{-1} \tag{23}$$

and the switching index $i$ governed by $i \in \{1,2\}$, together with (20).

The average dwell-time argument is a well-known approach toward stability analysis of time-dependent switched systems, see, e.g., [19]. In this approach, it is assumed that the system is able to switch to every mode of the system after a certain time. Stability is then proven by computing an average dwell time of how long the system should stay within a mode before a switch to another random mode occurs. Specifically, applying the average dwell-time method to our system yields a required average dwell time of at least 4.8 s per mode to guarantee stability. In practice, however, the breathing rate typically lies between 15 and 25 breaths per minute, which corresponds to $T_{\mathrm{insp}}$ and $T_{\mathrm{exp}}$ values between 1 and 2 s each (depending on the inspiration and expiration ratio). Thus, the dwell time required by the standard approach is significantly longer than the realistic inspiration and expiration intervals used in mechanical ventilation.

Therefore, we exploit the fact that the switching system in (22) contains two modes and is governed by a given time-dependent switching sequence [see (20)]. Using this information, we can pursue a stability analysis using less conservative, practically applicable, conditions compared to the average dwell-time argument. Therefore, we introduce Proposition 1, which presents a sufficient condition for the input-to-state stability of the closed-loop dynamics. Let us first formally introduce the input-to-state stability property [20].

*Definition 1:* System (22) is called input-to-state stable (ISS) if there exist functions $\gamma \in \mathcal{K}$ and $\beta \in \mathcal{KL}$ so that, for all initial conditions $x(0)$, all bounded inputs $r(t)$, and all times $t \geq 0$, the following inequality holds:

$$\|x(t)\| \leq \beta\left(\|x(0)\|, t\right) + \gamma\left(\sup_{0 \leq s \leq t} \|r(s)\|\right). \tag{24}$$

The following proposition is the main result to analyze stability of the closed-loop switched system.

*Proposition 1:* Consider the switching system in (20), (22), and (23). If there exist positive definite matrices $P_i = P_i^\top > 0$, $i = 1,2$, and $c_1 > 0$ such that the following inequalities hold:

$$A_{\mathrm{cl}}^{i\top} P_i + P_i A_{\mathrm{cl}}^i \leq -\epsilon P_i \quad \text{with } \epsilon > 0, \text{and for } i \in \{1,2\} \tag{25}$$

$$\mu_2 \mu_1 e^{-c_3 \bar{T}} < 1 \tag{26}$$

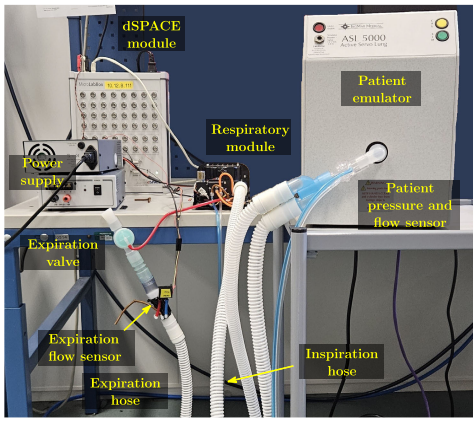


Fig. 4. Experimental setup consisting of the blower-driven ventilator, ASL 5000 breathing simulator, dSpace module, hose system, expiration valve, and expiration flow sensor.

where $c_3 := (1 - 1/c_1)\epsilon$, $\bar{T} = T_{\mathrm{insp}} + T_{\mathrm{exp}}$, $\mu_1 := \bar{\lambda}(P_2)/\underline{\lambda}(P_1)$, and $\mu_2 := \bar{\lambda}(P_1)/\underline{\lambda}(P_2)$, with $\bar{\lambda}(.)$ and $\underline{\lambda}(.)$, respectively, being the maximal and minimal eigenvalues of a symmetric, positive definite matrix, then the switching system is ISS.

*Proof:* See appendix. ∎

*Remark 1:* Note that the existence of $P_i$, $i = 1,2$, satisfying (25), is automatically guaranteed by the fact that the closed-loop systems in both modes are designed to be exponentially stable.

*Remark 2:* Note that ISS is established with respect to the reference $r$. This result can be readily extended to account for output disturbances $\tilde{n}$ by redefining the reference as $\bar{r} := r + \tilde{n}$. Similarly, the input disturbances $\tilde{d}$ can be accounted for by extending the state-space formulation to $\dot{x} = A_{\mathrm{cl}}^i x + B_{\mathrm{cl}}^i \bar{r} + B_{\tilde{d},\mathrm{cl}}^i \tilde{d}$ and applying similar reasoning as used in thepreceding ISS proof.

To assess the stability of the switched system, Proposition 1 must be checked for each plant realization separately. In Section IV, the control design procedure is applied to an experimental mechanical ventilator setup.

## IV. Decoupling-Based Controller Design in Mechanical Ventilation

A controller design that satisfies requirements 1) and 2) is presented in this section by following the design procedure, as presented in Section III. First, the experimental setup is introduced in Section IV-A. Second, in Section IV-B, the results of the plant identification and interaction analysis are discussed. Thereafter, the controller design is detailed in Section III-C, where the factorized Nyquist criterion is used to check the robustness against the residual interaction.

### A. Experimental Setup Description

The main components of the experimental setup are depicted in Fig. 4. The figure shows a Macawi blower-driven mechanical ventilation module (Demcon Macawi respiratory systems, Best, The Netherlands). Furthermore, the ASL5000[2]

[2]Trademarked.

TABLE I
DIFFERENT PATIENT CONFIGURATIONS THAT ARE USED

| **Patient configuration** (m) | **Lung resistance** [mbar s/ml] | **Lung compliance** [ml/mbar] | **Color index** |
|---|---|---|---|
| 1 | 5 | 20 | (—) |
| 2 | 5 | 50 | (—) |
| 3 | 20 | 20 | (—) |
| 4 | 50 | 20 | (—) |
| 5 | 50 | 10 | (—) |
| 6 | 20 | 10 | (—) |

Breathing Simulator (IngMar Medical, Pittsburgh, PA) is shown in Fig. 4. The breathing emulator is used to simulate a linear one-compartmental lung model, as described in [21]. In addition, a typical dual hose system used in a hospital setting is shown. At the end of the expiration hose, an expiration valve (GaleMed, Yilan, Taiwan) with an additional flow sensor is placed. The control and ventilation algorithms are implemented on a dSPACE system (dSPACE GmbH, Paderborn, Germany).

### B. System Identification and Interaction Analysis

The system $G$ (dynamics between inputs $u$ and outputs $y$; see Fig. 3) consists of the ventilator, patient, inspiration and expiration hose, piezo valve, and the expiration valve, as shown in Fig. 4. In this article, we emulate a set of adult patients from the ISO 80601 norm [22], leading to six different patient configurations $m \in \{1, 2, \ldots, 6\}$, as shown in Table I.

The plant $G_m$ of patient configuration $m$ is identified using two independent excitations [23]. These excitations identify each column of the process sensitivity $G_m S_m$ and sensitivity $S_m = 1/(1 + G_m)$ separately by injection of bandpass-filtered white noise on top of the plant input $u_1$ and $u_2$ (and measuring the resulting control output $u_1$ and $u_2$ and plant output $y_1$ and $y_2$, respectively). Then, the plant $G_m$ is obtained by performing

$$G_m(\omega_k) := G_m S_m(\omega_k) S_m(\omega_k)^{-1} \tag{27}$$

for the excitation frequency $\omega_k$ range of 0.1–60 Hz, which defines the region of interest. During identification, the pressure target is set to 5 mbar, and the baseflow target is set to 5 l/min.

The magnitude plots of the FRFs for all patient configurations are shown in Fig. 5. The outlet pressure ($y_1 = p_{\text{out}}$) and the outlet flow ($y_2 = Q_{\text{out}}$) are measured at the same location, as shown in Fig. 1. In general, we observe that all plant configurations exhibit approximately similar behavior. All FRFs have an approximate zero slope at low frequencies. Above 1 Hz, the patient dynamics start to play a significant role; hence, the patient configurations 1 and 2 start to deviate from the other configurations due to their lower lung resistance. The roll-off at higher frequencies (>10 Hz) is due to ventilator dynamics. In general, the FRFs from $u_2 = u_{\text{piezo}}$ to the outputs roll off at a lower frequency compared to those related to the first input $u_1$ (blower speed). These details are important for the interaction analysis that is described next.

In Fig. 6, the interaction indices for both systems $\underline{H}_m^i$, $i = 1, 2$ and $m \in \{1, 2, \ldots, 6\}$ are shown. For both systems, the interaction indices are not equal to zero on the displayed

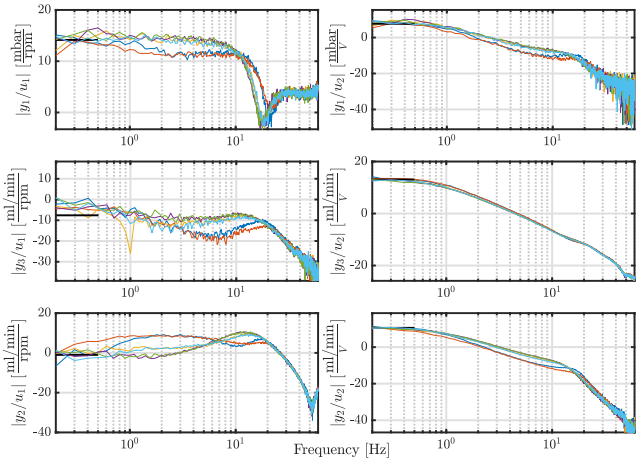


Fig. 5. FRF measurements of the plant $G_m$ with a set of different patients with $m \in \{1, \ldots, 6\}$. The colors in this figure match the colors as listed in Table I. The highlighted black part (—) is used for the static decoupling. The magnitude is plotted in decibels.

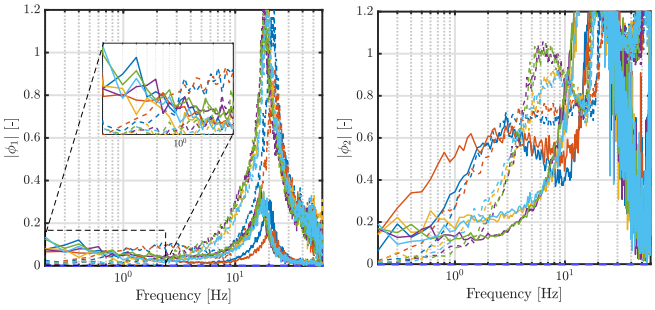


Fig. 6. Interaction index before and after static decoupling. In the left figure, the interaction index of $\underline{H}_m^1 = T_y^1 G_m(j\omega)$ (solid lines) and $H_m^1 = T_y^1 G_m(j\omega) T_u^1$ (dashed lines) is displayed for $m \in \{1, \ldots, 6\}$. In the right plot, the interaction index of $\underline{H}_m^2 = T_y^2 G_m(j\omega)$ (solid lines) and $H_m^2 = T_y^2 G_m(j\omega) T_u^2$ (dashed lines) is displayed for $m \in \{1, \ldots, 6\}$. The colors match with the color index in Table I.

frequency domain, i.e., interaction is present. The interaction of the plant $\underline{H}_m^1$ is smaller compared to plant $\underline{H}_m^2$ for $m \in \{1, 2, \ldots, 6\}$, which is predominantly caused by the sensor positions. In $\underline{H}_m^1$, the pressure and flow are measured at a different location, namely, $p_{\text{out}}$ and $Q_{\text{exp}}$, while, in $\underline{H}_m^2$, the pressure and flow are measured at the same position, namely, $p_{\text{out}}$ and $Q_{\text{out}}$, inherently leading to more coupling in the latter case. Again, the different plant configurations exhibit similar behavior, except for the plant configurations with patients 1 ($m = 1$) and 2 ($m = 2$) in system $\underline{H}_m^2$.

In Section III-C, a robust decentralized controller is designed for mechanical ventilation by following the approach presented in Section III.

### C. Controller Design

There are different ways to deal with the plant variety in control design. In this article, we do not incorporate the plant variety during design, but we choose a single plant variation to design $\tilde{K}_d^i$ and $T_u^i$ (with $i = 1, 2$) and subsequently analyze the stability and performance for all plant variations. The decision is made to design the controller around patient

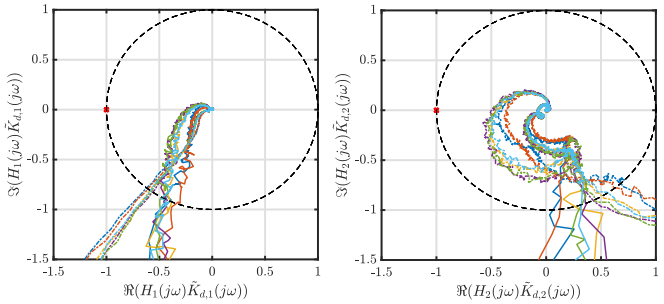

Fig. 7. Nyquist plots of the open-loop SISO systems for both systems and all patient configurations. The different patient configurations match the color index in Table I. The solid lines represent the $H_m^{i,11}\tilde{K}_d^{i,11}$ systems, and the dashed lines represent the $H_m^{i,22}\tilde{K}_d^{i,22}$ systems. All individual SISO systems are closed-loop stable based on the Nyquist plots. The dashed line (- - -) represents the unit circle.

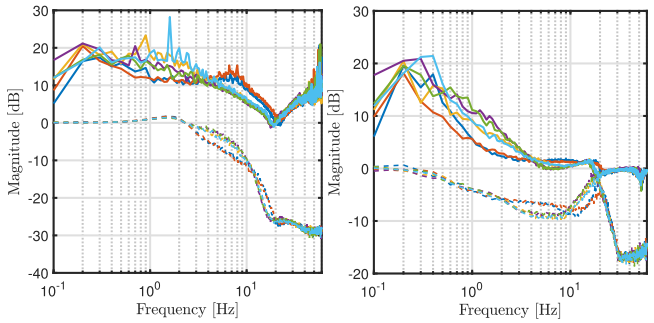

Fig. 8. Stability and robustness assessment using the factorized Nyquist criterion, with $H_m^1(j\omega) = T_y^1 G_m(j\omega) T_u^1$ system on the left and the $H_m^2(j\omega) = T_y^2 G_m(j\omega) T_u^2$ system on the right. The solid lines represent $\mu_{\tilde{\mathcal{T}}}^{-1}(E)$, and the dashed lines are the maximum singular value $\bar{\sigma}(\tilde{\mathcal{T}}) = \sup_i \tilde{\mathcal{T}}^{ii}$ based on the diagonal elements of $\tilde{\mathcal{T}}$. To check the condition in (15), one must compare the solid line and the dashed line of the same color. The colors match with the color index in Table I.

configuration 3 ($m = 3$) because this patient configuration is the best representation of the "average" patient. This plant is defined as $G_{\text{nom}} := G_3$.

Following the control procedure in Section III, interaction is reduced below the bandwidth (which is required to be between 1 and 2 Hz) by designing a static decoupling for plant $\underline{H}_m^1$ and $\underline{H}_m^2$. Decoupling around the static gain results in the most reduction of the interaction index because it has a zero slope in this frequency range and the variation between plants is low. The improved interaction indices for $H_m^i = T_y^i G_m T_u^i$ with $i \in \{1, 2\}$ and $m \in \{1, 2, \ldots, 6\}$ are shown in Fig. 6 (the dashed lines). For both systems $H_m^1$ and $H_m^2$, the interaction index decreases below the bandwidth (approx. 2 Hz) for all patient configurations $m \in \{1, 2, \ldots, 6\}$. This shows that it is possible to use a single static decoupling matrix (designed for the average patient) for all plant configurations. Nevertheless, it can also be seen that the interaction reduces most for the patient configurations that are most similar to the plant of the average patient $G_{\text{nom}}$.

Due to the dynamics of the plant, i.e., different slopes because of the roll-off, it is only possible to decrease interaction locally in the (low) frequency domain. Static decoupling decreases interaction at low frequencies but increases interaction above 2 Hz. Static decoupling does not decrease the two-way interaction sufficiently in the whole frequency range. Therefore, it is decided to still take the interaction into account during (robust) decentralized controller design with the help of the factorized Nyquist criterion as is presented in the control design procedure.

Two decentralized PI controllers

$$\tilde{K}_d^1(s) = \begin{bmatrix} \frac{20}{s} + 0.1 & 0 \\ 0 & \frac{20}{s} + 1.5 \end{bmatrix} \text{ and}$$
$$\tilde{K}_d^2(s) = \begin{bmatrix} \frac{5}{s} + 0.5 & 0 \\ 0 & \frac{3}{s} + 2 \end{bmatrix} \tag{28}$$

are designed to stabilize the systems $H_m^1$ and $H_m^2$ with $m \in \{1, 2, \ldots, 6\}$, respectively. Due to the system dynamics, the PI controllers $\tilde{K}_d^i$ (independent of the patient) already stabilize the systems and satisfy the rules of thumb for the robustness margins regarding controller design as visualized by the Nyquist plots in Fig. 7.

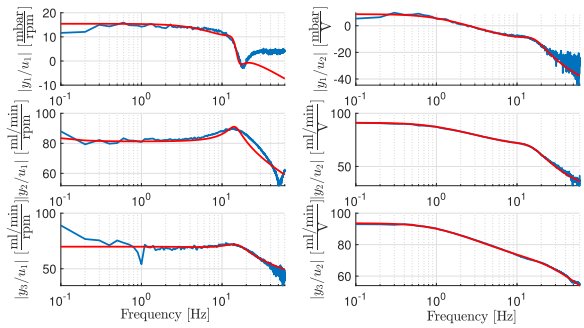

Fig. 9. Frequency response measurements of the unscaled plant $G_{\text{nom}}$ together with a fit (—). The magnitude is plotted in decibels.

In Fig. 8, it is shown that the factorized Nyquist criterion in (15) is satisfied for all $H_m^1$ and $H_m^2$ with $m \in \{1, 2, \ldots, 6\}$; hence, the MIMO controllers for the individual systems are stable. The six different patient configurations are a good indication for the expected patients; however, a conservative design with large robustness margins is presented such that the controllers are also stable for unexpected patients outside the tested variations.

While the individual systems are stable, this does not guarantee closed-loop stability of the overall system (which contains a switch). Therefore, we use Proposition 1 to prove stability of the switched system. Solving the linear matrix inequalities in (25) requires a state-space representation of the plant. The state-space representation of the plant is obtained by making strictly proper fits of the single-input–single-output transfer functions of the nominal plant, as shown in Fig. 9. The fits are obtained by minimizing the output error between the fit plant model $\hat{G}_{\text{nom}}(s = j\omega)$ and the measured FRF data $G_{\text{nom}}(j\omega)$ over the frequency range of 0.1–60 Hz, using a least-squares approach applied to each individual transfer function.

A nominal plant fit was obtained using this approach. The resulting strictly proper transfer functions consist of eight poles and seven zeros, selected to accurately capture the dynamic behavior of the measured FRFs while maintaining a low-order structure suitable for stability analysis.

The model selection and validation were performed via manual inspection of the fit quality, focusing on minimizing

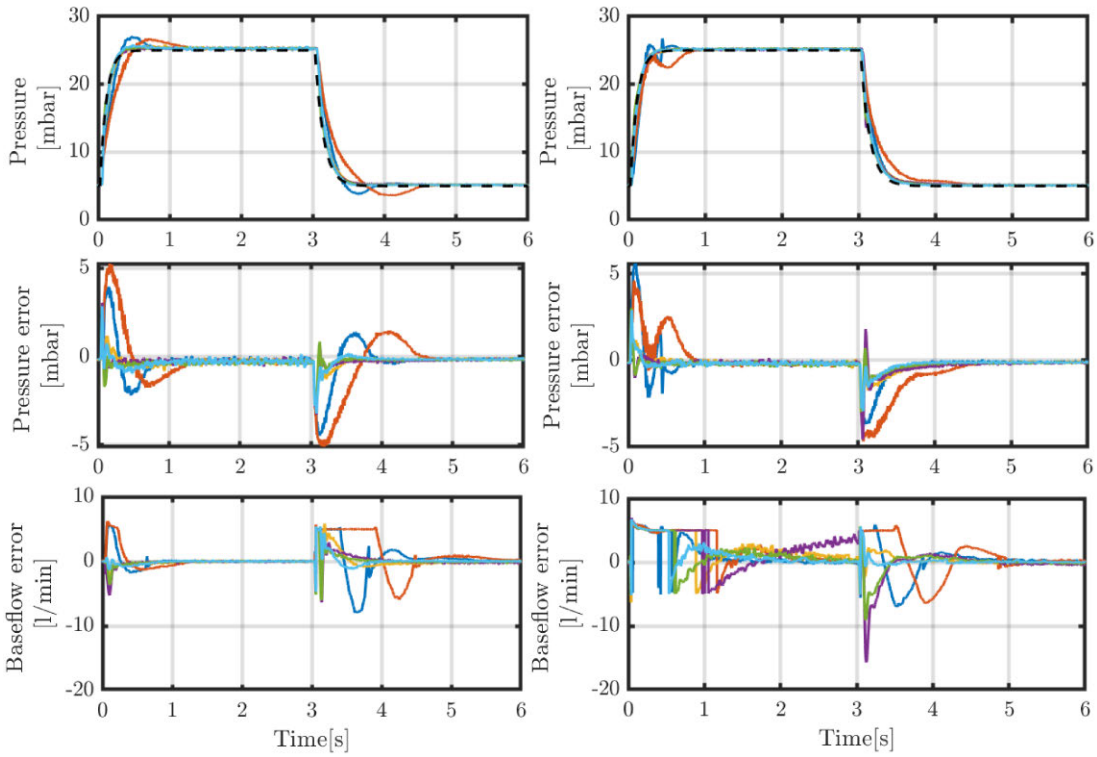


Fig. 10. Comparison of the time-domain results of the proposed controller (left) and the SOP controller (right) regarding the pressure tracking of a single breath with the accompanying pressure and baseflow errors. The pressure target is displayed as (- - -) in the top plot, and the colors match the color index in Table I. The proposed controller reduces the baseflow error significantly compared to the state-of-the-practice controller.

frequency deviations around the bandwidth and ensuring physical plausibility. The current fits show consistent and reliable behavior, which supports confidence in the switching performance. Small deviations from the measured model occur at high frequencies between the transfer of $y_1$ to $u_1$, and $y_2$ to $u_1$. From a dynamics perspective, all plants should be strictly proper because we expect no feed through based on the actuator and sensor pairs. Furthermore, the $y_1$ to $u_1$ transfer decreases after 60 Hz.

With the model fit, a state-space representation of the closed-loop system is found by using (22) and (23). Solving the LMIs gives us a value of $\epsilon = 2.0$, resulting in $c_3 = (1 - 1/c_1)\epsilon$ with $c_1 = 100$. If we fill in $T_{\text{insp}} = T_{\text{exp}} = 3$ with $c_3$ that is found by solving the LMIs, all conditions in Proposition 1 are satisfied. This means that the nominal system is ISS for the time-switching strategy as presented in (20).

## V. Results of Experimental Case Study

In the experimental case study, a real mechanical ventilator and a lung emulator are used to analyze the tracking performance of the designed controller with the proposed methodology. The tracking performance in the time domain is analyzed for the entire set of patient configurations, as shown in Table I.

The control strategy designed in Section IV is implemented in the experimental setup of Fig. 4. The tracking performance of the designed controller is compared to the state-of-practice (SOP) controller that only uses the outlet pressure $p_{\text{out}}$ and the outlet flow $Q_{\text{out}}$ sensors, thus making it impossible to track the baseflow during inspiration. Furthermore, the SOP controller ignored interaction during design.

The results of the pressure tracking of a patient's breath for both control strategies are shown in top plots of Fig. 10, and the tracking errors are shown in the bottom two plots of those figures. Both control strategies show accurate tracking of the pressure and flow targets. The proposed controller converges to the baseflow reference faster with more smooth inputs compared to the SOP controller due to the proposed switching strategy. The SOP controller fully closes the valve during the first phase of the breath because the baseflow cannot be tracked, hence introducing discontinuities in the baseflow $Q_{\text{bf}}$. The patient configurations 1 and 2 are most challenging to track for both controllers due to the lung characteristics, i.e., large lungs with a low airway resistance. These lung characteristics enforce large expiration flows, leading to a flow spill in the inspiration hose, which results in large baseflow errors.

The pressure errors during pressure build-up and decrease are slightly larger for the proposed method compared to the SOP, as shown in Fig. 10. To quantify the performance, the root mean square error (RMSE) for the SOP and the decentralized controller for the different patients is shown in Table II. The base flow error of the proposed method is improved for all patients compared to the SOP controller. The proposed method is able to track the baseflow in the first phase of a breath, and the overshoot during expiration is decreased. In general, we conclude that the tracking performance is better compared to the SOP because the additional benefits of

TABLE II
COMPARISON OF THE RMSES FOR A BREATHING CYCLE FOR THE SOP CONTROLLER AND THE PROPOSED STATE-OF-THE-ART (SOA) CONTROLLER

| Patient config. | $\|e_p\|_2$ SOP [mbar] | $\|e_p\|_2$ SOA [mbar] | $\|e_Q\|_2$ SOP [l/min] | $\|e_Q\|_2$ SOA [l/min] |
|---|---|---|---|---|
| 1 | 0.992 | 1.049 | 2.456 | 2.097 |
| 2 | 1.312 | 1.567 | 3.158 | 2.471 |
| 3 | 0.477 | 0.464 | 2.292 | 1.012 |
| 4 | 0.482 | 0.416 | 3.096 | 0.897 |
| 5 | 0.393 | 0.410 | 2.162 | 0.745 |
| 6 | 0.396 | 0.439 | 1.745 | 0.746 |

improved flow tracking, e.g., better flushing of the hose and more calm pressure and flow signals, outweigh the decrease in pressure tracking performance, which does not have negative effects for the patient. Furthermore, the proposed controller, designed based on a single patient configuration, results in improved performance for all patient configurations.

## VI. CONCLUSION AND RECOMMENDATIONS

The presented controller framework in this article improves the baseflow tracking in mechanical ventilation. This is achieved by addressing interactions within mechanical ventilation and designing a switching strategy. A control strategy that uses static decoupling combined with factorized Nyquist to design a decentralized controller is presented. To track the baseflow in all phases of breathing, a switching strategy is designed that switches between two flow sensors during a single patient breath. Furthermore, it is experimentally shown that the proposed strategy significantly improves baseflow tracking performance for a range of patients while only insignificantly decreasing the pressure tracking performance for all patients. The proposed controller designed for a single patient is robust for the different patient variations. Concluding, the proposed method indicates that switching between flow sensors results in improved tracking performance in mechanical ventilation.

The tracking performance of the pressure can still be improved. A complete, robust or adaptive, design approach can be taken to improve performance for the entire range of patients. A robust approach also requires extending Proposition 1 to address model uncertainties. Furthermore, learning controllers can exploit the repetitive nature of breathing and thereby learn repetitive disturbances over multiple cycles to further improve the tracking. Future research also includes exploring methods for frequency-based techniques to assess the stability of switched systems to have a fully frequency-based approach. Another important aspect that needs further research is the spontaneous breathing of patients. This research focused on sedated (passive) patients, but, as soon as the patient starts breathing actively, an additional "disturbance" enters the system. For the patient's comfort, it is necessary that these disturbances are taken into account.

## APPENDIX A

### A. Proof Proposition 1

The proof comprises two main steps. First, we consider the individual subsystems of (22) and show that each of them is ISS, characterized by individual ISS Lyapunov function inequalities. Using these results, we, second, construct an upper bound on the state evolution $x(t)$ and show that this bound ensures ISS of the switching closed-loop system.

Consider the switching system in (22). First, we exploit that the dynamics in each mode ($i = 1$ and $i = 2$) are ISS following the results from [20]. Indeed, the individual modes in the system in (22) are ISS if they admit an ISS-Lyapunov function. Consider the candidate ISS-Lyapunov function $V_i(x)$ as

$$V_i(x) := x^\top P_i x \tag{29}$$

where $P_i$, $i = 1, 2$, are symmetric positive definite matrices satisfying (25), which exist because $A^i_{\mathrm{cl}}$ is Hurwitz for $i \in \{1, 2\}$. Each ISS-Lyapunov function is bounded by

$$\alpha_{1,i}(\|x\|) \le V_i(x) \le \alpha_{2,i}(\|x\|) \tag{30}$$

where $\alpha_{1,i}(\|x\|) := \underline{\lambda}(P_i)\|x\|^2$ and $\alpha_{2,i}(\|x\|) := \bar{\lambda}(P_i)\|x\|^2$. The time derivative of the ISS-Lyapunov functions, along the dynamics in (22) within each individual mode, is equal to

$$\dot{V}_i(x) = x^\top \left(P_i A^i_{\mathrm{cl}} + A^{i\top}_{\mathrm{cl}} P_i\right) x + 2x^\top P_i B^i_{\mathrm{cl}} r. \tag{31}$$

Given (25) in the proposition, the time-derivative of the ISS-Lyapunov function is upper bounded as

$$\begin{aligned}
\dot{V}_i(x) &\le x^\top (-\epsilon P_i)\, x + 2\, x^\top P_i B^i_{\mathrm{cl}} r \\
&\le -\epsilon V_i(x) + 2\|x\|_{P_i} \left\| B^i_{\mathrm{cl}} r \right\|_{P_i} \\
&\le -\epsilon V_i(x) + \frac{\epsilon}{c_1}\underline{\lambda}(P_i)\|x\|^2 + \frac{c_1 \bar{\lambda}^2(P_i)}{\epsilon \underline{\lambda}(P_i)} \left\| B^i_{\mathrm{cl}} r \right\|^2 \\
&\le -\alpha_{3,i}(V_i(x)) + \alpha_{4,i}(\|r\|)
\end{aligned} \tag{32}$$

where $\|x\|^2_{P_i} = x^T P_i x$, $c_1 > 0$ is a user-defined constant, and $\alpha_{3,i}(V_i(x)) := c_3 V_i(x)$ and $\alpha_{4,i}(\|r\|) := c_{4,i}\|r\|^2$, which are both class $\mathcal{K}$-functions with $c_3 := c_2\epsilon$ and $c_{4,i} := (c_1\bar{\lambda}^2(P_i))/(\epsilon\underline{\lambda}(P_i))\|B^i_{\mathrm{cl}}\|^2$, and $c_2 := (1 - 1/c_1)$. The inequality $2\|x\|_{P_i}\|B^i_{\mathrm{cl}} r\|_{P_i} \le \epsilon/(c_1)\|x\|^2_{P_i} + (c_1)/\epsilon\|B^i_{\mathrm{cl}} r\|^2_{P_i}$ follows from Young's inequality and is used to derive the third line in (32).

Using the comparison lemma (see [24]), we find that

$$V_i(t) \le V_i(t_0)\, e^{-c_3 t} + \frac{c_{4,i}}{c_3}\left(1 - e^{-c_3 t}\right) \sup_{t_0 \le \tau \le t} \|r(\tau)\|^2 \tag{33}$$

holds for the dynamics of the individual modes, i.e., $i = 1, 2$.

Let us now revert to the stability analysis of the switching system and consider the function

$$V(t) = V_{i(t)}(t) \tag{34}$$

where $i$ is defined by the switching strategy in (20), as a candidate ISS Lyapunov function for the switched system. See an exemplary evolution of this function in Fig. 11.

To construct an upper bound for the evolution of $V(t)$, we first analyze: 1) how $V_1$ evolves from the beginning of an inspiration phase, in which $i = 1$, to the beginning of the next inspiration phase and 2) how $V_2$ evolves from the beginning of an expiration phase, in which $i = 2$, to the beginning of the next expiration phase. Let $\bar{T} := T_{\mathrm{insp}} + T_{\mathrm{exp}}$ be the length of one breath, and let us define the evolution of $V_1$ from an inspiration phase with index $k$ to the next inspiration phase

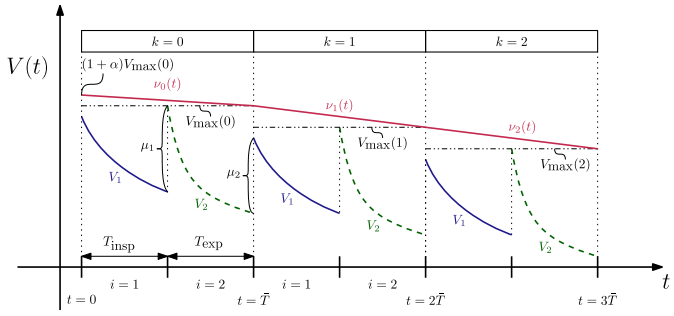


Fig. 11. Schematic overview of the Lyapunov function over time with the constructed upper bound $\nu_k$(t) in red.

with index $k+1$ (from the beginning of the blue curve to the beginning of the next blue curve in Fig. 11), which results in

$$V_1\left((k+1)\bar{T}\right) \le \mathcal{A}e^{-c_3\bar{T}}V_1\left(k\bar{T}\right) + \mathcal{B}_1 \sup_{k\bar{T}\le\tau\le(k+1)\bar{T}} \|r(\tau)\|^2 \tag{35}$$

where $\mathcal{A} := \mu_2\mu_1$ and $\mathcal{B}_1 := \mu_2\mu_1(c_{4,1})/(c_3)e^{-c_3T_{\text{exp}}} - \mu_2\mu_1(c_{4,1})/(c_3)e^{-c_3\bar{T}} - \mu_2(c_{4,2})/(c_3)e^{-c_3T_{\text{exp}}} + \mu_2(c_{4,2})/(c_3)$. In the derivation of (35), we exploited (33) (for $i=1$ and $i=2$) and (30).

Again, (33) (for $i=1$ and $i=2$) and (30) are exploited for $V_2$ from the beginning of an expiration to beginning of the next expiration (from the beginning of a green curve to the start of the next green curve in Fig. 11), which gives

$$V_2\left((k+1)\bar{T}+T_{\text{insp}}\right) \le \mathcal{A}e^{-c_3\bar{T}}V_2\left(k\bar{T}+T_{\text{insp}}\right) + \mathcal{B}_2 \sup_{k\bar{T}+T_{\text{insp}}\le\tau\le(k+1)\bar{T}+T_{\text{insp}}} \|r(\tau)\|^2 \tag{36}$$

where $\mathcal{B}_2 := \mu_1\mu_2(c_{4,2})/(c_3)e^{-c_3T_{\text{insp}}} - \mu_1\mu_2(c_{4,2})/(c_3)e^{-c_3\bar{T}} - \mu_1(c_{4,1})/(c_3)e^{-c_3T_{\text{insp}}} + \mu_1(c_{4,1})/(c_3)$.

Next, we analyze the evolution of the Lyapunov functions $V_1$ and $V_2$ from, respectively, $t=0$ and $t=T_{\text{insp}}$ the start to, respectively, the start of the $k$th inspiration and the $k$th expiration as follows:

$$V_1\left(k\bar{T}\right) \le \mathcal{A}^k e^{-kc_3\bar{T}}V_1(0) + \sum_{j=0}^{k-1}\mathcal{A}^j e^{-jc_3\bar{T}}\mathcal{B}_1 \sup_{0\le\tau\le\bar{T}} \|r(\tau)\|^2 \tag{37}$$

for $k=1,2,3,\ldots$, and

$$V_2\left(k\bar{T}+T_{\text{insp}}\right) \le \mathcal{A}^k e^{-kc_3\bar{T}}V_2\left(T_{\text{insp}}\right) + \sum_{j=0}^{k-1}\mathcal{A}^j e^{-jc_3\bar{T}}\mathcal{B}_2 \sup_{0\le\tau\le\bar{T}} \|r(\tau)\|^2 \tag{38}$$

for $k=1,2,3,\ldots$. Note that the reference signal $r(t)$ is periodic; hence,

$$\sup_{k\bar{T}\le\tau<(k+1)\bar{T}} \|r(\tau)\|^2 = \sup_{0\le\tau\le\infty} \|r(\tau)\|^2 \text{ for all } k=0,1,2,\ldots. \tag{39}$$

Now, an upper bound $\nu(t)$ on $V(t)$ in (34) is constructed. Define

$$V_{\max}(k) := \max\left(V_1\left(k\bar{T}\right), V_2\left(k\bar{T}+T_{\text{insp}}\right)\right) \text{ for } k=0,1,2,\ldots \tag{40}$$

and define

$$\nu(t) = \nu_k(t) \text{ for } t\in\left[k\bar{T},(k+1)\bar{T}\right) \text{ for } k=0,1,2,\ldots \tag{41}$$

with

$$\nu_0(t) := -\frac{(1+\alpha)V_{\max}(0)-V_{\max}(0)}{\bar{T}}t + V_{\max}(0)(1+\alpha) \tag{42}$$

for $t\in[0,\bar{T})$ with $\alpha>0$, and

$$\nu_k(t) := \frac{V_{\max}(k)-V_{\max}(k-1)}{\bar{T}}\left(t-k\bar{T}\right) + V_{\max}(k-1) \tag{43}$$

for $t\in[k\bar{T},(k+1)\bar{T})$ and for $k=1,2,3\ldots,$. Herein, $\nu_k(t)$ be an upper-bound for $V(t)$ within the $k$th interval (see the red piecewise linear function in Fig. 11). This results in the upper bound $V(t)\le\nu(t)\ \forall t\ge 0$. Next, combining (37), (38), and (40) yields

$$V_{\max}(k) \le \max_{i\in\{1,2\}}\left\{\mathcal{A}^k e^{-kc_3\bar{T}}V_{\max}(0) + \sum_{j=0}^{k-1}\mathcal{A}^j e^{-jc_3\bar{T}}\mathcal{B}_i \sup_{0\le\tau\le t}\|r(\tau)\|^2\right\} \tag{44}$$

$$\Upsilon\left(V_1(0), t, \sup_{0\le\tau\le t}\|r(\tau)\|\right) := \begin{cases} -\frac{\alpha\left(\bar{c}_5V_1(0)+\bar{c}_6\sup_{0\le\tau\le\bar{T}}\|r(\tau)\|^2\right)}{\bar{T}}t + (1+\alpha)\left(\bar{c}_5V_1(0)+\bar{c}_6\sup_{0\le\tau\le t}\|r(\tau)\|^2\right) & \text{for } t\in\left[k\bar{T},(k+1)\bar{T}\right) \text{ with } k=0 \\ \left(1+\frac{1}{\bar{T}}\left(\mathcal{A}e^{-c_3\bar{T}}-1\right)(t-\bar{T})\right)\left(\bar{c}_5V_1(0)+\bar{c}_6\sup_{0\le\tau\le t}\|r(\tau)\|^2\right) & \\ +\frac{1}{\bar{T}}\bar{\mathcal{B}}(t-\bar{T})\sup_{0\le\tau\le t}\|r(\tau)\|^2 & \text{for } t\in\left[k\bar{T},(k+1)\bar{T}\right) \text{ with } k=1 \\ \left(\frac{1}{\bar{T}}\left(\mathcal{A}e^{-c_3\bar{T}}-1\right)\mathcal{A}^{k-1}e^{-(k-1)c_3\bar{T}}(t-k\bar{T})\right)\left(\bar{c}_5V_1(0)+\bar{c}_6\sup_{0\le\tau\le t}\|r(\tau)\|^2\right) & \\ +\mathcal{A}^{k-1}e^{-(k-1)c_3\bar{T}}\left(\bar{c}_5V_1(0)+\bar{c}_6\sup_{0\le\tau\le t}\|r(\tau)\|^2\right) & \\ +\frac{1}{\bar{T}}\mathcal{A}^{k-1}e^{-(k-1)c_3\bar{T}}\bar{\mathcal{B}}\sup_{0\le\tau\le t}\|r(\tau)\|^2(t-k\bar{T}) & \text{for } t\in\left[k\bar{T},(k+1)\bar{T}\right) \text{ with } k=2,3,4,\ldots \\ +\sum_{j=0}^{k-2}\mathcal{A}^j e^{-jc_3\bar{T}}\bar{\mathcal{B}}\sup_{0\le\tau\le t}\|r(\tau)\|^2 & \end{cases} \tag{47}$$

$$\gamma\left(\sup_{0\le\tau\le t}\|r(\tau)\|\right) := \frac{1}{\sqrt{c_\lambda}}\max\left\{\sqrt{(1+\alpha)\,\bar{c}_6},\ \sqrt{\frac{\bar{\mathcal{B}}}{1-\mathcal{A}e^{-c_3\bar{T}}}+\bar{c}_6}\right\}\sup_{0\le\tau\le t}\|r(\tau)\| \tag{51}$$

$$\beta(\|x(0)\|,t) := \begin{cases} \dfrac{\sqrt{\bar{\lambda}(P_1)}}{\sqrt{c_\lambda}}\sqrt{(1+\alpha)\,\bar{c}_5-\dfrac{1}{\bar{T}}\alpha\bar{c}_5 t}\,\|x(0)\| & \text{for } t\in\left[k\bar{T},(k+1)\,\bar{T}\right) \text{ with } k=0 \\ \dfrac{\sqrt{\bar{\lambda}(P_1)}}{\sqrt{c_\lambda}}\sqrt{\bar{c}_5\left(1+\dfrac{1}{\bar{T}}\left(\mathcal{A}e^{-c_3\bar{T}}-1\right)\left(t-\bar{T}\right)\right)}\,\|x(0)\| & \text{for } t\in\left[k\bar{T},(k+1)\,\bar{T}\right) \text{ with } k=1 \\ \dfrac{\sqrt{\bar{\lambda}(P_1)}}{\sqrt{c_\lambda}}\sqrt{\bar{c}_5\left(\dfrac{1}{\bar{T}}\left(\mathcal{A}e^{-c_3\bar{T}}-1\right)\mathcal{A}^{k-1}e^{-(k-1)c_3\bar{T}}\left(t-k\bar{T}\right)+\mathcal{A}^{k-1}e^{-(k-1)c_3\bar{T}}\right)}\,\|x(0)\| & \text{for } t\in\left[k\bar{T},(k+1)\,\bar{T}\right) \text{ with } k=2,3,4,\ldots \end{cases} \tag{52}$$

for $k = 1, 2, 3, \ldots,$. Furthermore, we know that

$$V_{\max}(0) \le \max_{i\in\{1,2\}}\left(c_{5,i}V_1(0) + c_{6,i}\sup_{0\le\tau\le t}\|r(\tau)\|^2\right) \tag{45}$$

where $c_{5,1} := 1$, $c_{5,2} := \mu_1 e^{-c_3 T_{\text{insp}}}$, $c_{6,1} := 0$, and $c_{6,2} := \mu_1(c_{4,1})/(c_3)(1-e^{-c_3 T_{\text{insp}}})$; hence, we define the following bound on $V(t)$ by using (41), (44), and (45), which gives that:

$$V(t) \le \Upsilon\left(V_1(0), t, \sup_{0\le\tau\le t}\|r(\tau)\|\right) \tag{46}$$

where $\Upsilon(V_1(0), t, \sup_{0\le\tau\le t}\|r(\tau)\|)$ is defined in (47), as shown at the bottom of the previous page, where $\bar{\mathcal{B}} := \max_{i\in\{1,2\}}\mathcal{B}_i$, $\bar{c}_5 := c_{5,i^*}$, and $\bar{c}_6 := c_{6,i^*}$ with

$$i^* = \arg\max_{i\in\{1,2\}}(c_{5,i}V_1(0) + c_{6,i}\sup_{0\le\tau\le t}\|r(\tau)\|^2). \tag{48}$$

Next, it holds that

$$\|x(t)\|^2 \le \frac{1}{c_\lambda}V(t) \tag{49}$$

where $i \in 1, 2$ and $c_\lambda := \min_{i\in\{1,2\}}\underline{\lambda}(P_i)$, leading to

$$\|x(t)\| \le \sqrt{\frac{1}{c_\lambda}}\sqrt{\Upsilon\left(\bar{\lambda}(P_1)\|x(0)\|^2, t, \sup_{0\le\tau\le t}\|r(\tau)\|\right)} \tag{50}$$

with $i \in \{1, 2\}$ and $\bar{\lambda}(P_1)$ being the maximum eigenvalue of $P_1$. Using that $(a + b)^{1/2} \le \sqrt{a} + \sqrt{b}$ and substituting (47) into (50) give that we can conclude that (24) holds, with

$\gamma(\sup_{0\le\tau\le t}\|r(\tau)\|)$ as defined in (51), as shown at the top of the page, where it is used that (26) holds such that

$$\sum_{j=0}^{k-1}\mathcal{A}^j e^{-jc_3\bar{T}}\bar{\mathcal{B}} \le \sum_{j=0}^{\infty}\mathcal{A}^j e^{-jc_3\bar{T}}\bar{\mathcal{B}} = \frac{\bar{\mathcal{B}}}{1-\mathcal{A}e^{-c_3\bar{T}}} \tag{53}$$

and $\beta(\|x(0)\|, t)$ as (52), as shown at the top of the page. We observe that $\gamma(0) = 0$, and it is strictly increasing, so $\gamma \in \mathcal{K}$. Furthermore, $\beta(0, t) = 0$, $\beta(\|x(0)\|, t)$ is strictly increasing in $\|x(0)\|$, and $\beta(\|x(0)\|, t)$ is continuously decreasing in its second argument if $\mathcal{A}e^{-c_3\bar{T}} < 1$ (which follows from the condition (26) in the proposition) and if $t \to \infty$ then $\lim_{t\to\infty}\beta(\|x(0)\|, t) \to 0$, so $\beta \in \mathcal{KL}$. Hereby, the proof is completed using Definition 1.

## REFERENCES


[1] M. A. Warner and B. Patel, *Mechanical Ventilation*, 3rd ed., Amsterdam, The Netherlands: Elsevier, 2013.

[2] H. Wunsch, W. T. Linde-Zwirble, D. C. Angus, M. E. Hartman, E. B. Milbrandt, and J. M. Kahn, "The epidemiology of mechanical ventilation use in the United States," *Crit. Care Med.*, vol. 38, no. 10, pp. 1947–1953, Oct. 2010.

[3] M. J. Tobin, *Principle and Practice of Mechanical Ventilation*, 3rd ed., New York, NY, USA: McGraw-Hill, 2013.

[4] B. Hunnekens, S. Kamps, and N. Van De Wouw, "Variable-gain control for respiratory systems," *IEEE Trans. Control Syst. Technol.*, vol. 28, no. 1, pp. 163–171, Jan. 2020.

[5] L. Blanch et al., "Asynchronies during mechanical ventilation are associated with mortality," *Intensive Care Med.*, vol. 41, no. 4, pp. 633–641, Apr. 2015.

[6] M. A. Borrello, "Adaptive inverse model control of pressure based ventilation," in *Proc. Amer. Control Conf.*, vol. 2, 2001, pp. 1286–1291.

[7] H. Li and W. M. Haddad, "Model predictive control for a multicompartment respiratory system," *IEEE Trans. Control Syst. Technol.*, vol. 21, no. 5, pp. 1988–1995, Sep. 2013.

[8] J. Reinders, B. Hunnekens, F. Heck, T. Oomen, and N. van de Wouw, "Adaptive control for mechanical ventilation for improved pressure support," *IEEE Trans. Control Syst. Technol.*, vol. 29, no. 1, pp. 180–193, Jan. 2021.

[9] M. Scheel, A. Berndt, and O. Simanski, "Iterative learning control: An example for mechanical ventilated patients," *IFAC-PapersOnLine*, vol. 48, no. 20, pp. 523–527, 2015, doi: 10.1016/j.ifacol.2015.10.194.

[10] A. F. de Castro and L. A. B. Tôrres, "Iterative learning control applied to a recently proposed mechanical ventilator topology," *IFAC-PapersOnLine*, vol. 52, no. 1, pp. 154–159, 2019.

[11] J. Reinders, R. Verkade, B. Hunnekens, N. van de Wouw, and T. Oomen, "Improving mechanical ventilation for patient care through repetitive control," *IFAC-PapersOnLine*, vol. 53, no. 2, pp. 1415–1420, 2020, doi: 10.1016/j.ifacol.2020.12.1906.

[12] J. Reinders, M. Giaccagli, B. Hunnekens, D. Astolfi, T. Oomen, and N. van de Wouw, "Repetitive control for Lur'e-type systems: Application to mechanical ventilation," *IEEE Trans. Control Syst. Technol.*, vol. 31, no. 4, pp. 1819–1829, Jul. 2023.

[13] S. Skogestad and I. Postletwaite, *Multivariable Feedback Control*. Hoboken, NJ, USA: Wiley, 2006.

[14] T. Oomen, "Advanced motion control for precision mechatronics: Control, identification, and learning of complex systems," *IEEJ J. Ind. Appl.*, vol. 7, no. 2, pp. 127–140, 2018.

[15] L. Van De Kamp, I. Franklin, B. Van Loon, T. Oomen, and N. Van De Wouw, "MIMO-decoupling to improve pressure and flow tracking in mechanical ventilation," in *Proc. Amer. Control Conf. (ACC)*, Jul. 2025, pp. 1009–1014.

[16] E. Bristol, "On a new measure of interaction for multivariable process control," *IEEE Trans. Autom. Control*, vol. AC-11, no. 1, pp. 133–134, Jan. 1966.

[17] P. Grosdidier and M. Morari, "Interaction measures for systems under decentralized control," *Automatica*, vol. 22, no. 3, pp. 309–319, May 1986.

[18] G. Zames, "On the input–output stability of time-varying nonlinear feedback systems part one: Conditions derived using concepts of loop gain, conicity, and positivity," *IEEE Trans. Autom. Control*, vol. AC-11, no. 2, pp. 228–238, Apr. 1966.

[19] D. Liberzon, *Switching in Systems and Control*. Cham, Switzerland: Springer, 2003.

[20] E. D. Sontag and Y. Wang, "On characterizations of the input-to-state stability property," *Syst. Control Lett.*, vol. 24, no. 5, pp. 351–359, Apr. 1995.

[21] J. H. T. Bates, *Lung Mechanics: An Inverse Modeling Approach*. Cambridge, U.K.: Cambridge Univ. Press, 2009.

[22] *Medical Electrical Equipment–Part 2-12: Particular Requirements for Basic Safety and Essential Performance of Critical Care Ventilators*, Standard NEN-EN-ISO 80601-2-12, 2011.

[23] E. Evers, R. Voorhoeve, and T. Oomen, "On frequency response function identification for advanced motion control," in *Proc. IEEE 16th Int. Workshop Adv. Motion Control (AMC)*, Sep. 2020, pp. 1–6.
[24] H. K. Khalil, *Nonlinear Systems*. Upper Saddle River, NJ, USA: Prentice-Hall, 2002.

**Lars van de Kamp** received the B.Sc. degree in mechanical engineering from Eindhoven University of Technology, Eindhoven, The Netherlands, in 2019, and the M.Sc. degree in mechanical engineering (cum laude) from Eindhoven University of Technology in 2021, where he is currently pursuing the Ph.D. degree with the Dynamics and Control Group.

His M.Sc. graduation work on "Patient-Ventilator Asynchrony Detection and Classification Within Mechanical Ventilation" was awarded the M.Sc. thesis award (Mechanical Engineering). His current research interests include system identification, and interpretable data-driven and machine learning techniques and control, with application to mechanical ventilation.

**Isabelle Franklin** received the B.Sc. (cum laude) and M.Sc. degrees in mechanical engineering, with a focus on control systems, from Eindhoven University of Technology, Eindhoven, The Netherlands, in 2024.

Her M.Sc. research, titled "an MIMO Approach to Pressure and Flow Control in Mechanical Ventilation Static Decoupling," was conducted in collaboration with DEMCON Eindhoven. She began her professional career in 2024 as a Mechatronic Systems Engineer at DEMCON Life Sciences and Health and is still affiliated with topics such as control for medical systems.

**Bas van Loon** received the M.Sc. and Ph.D. degrees in mechanical engineering, with a focus on control systems technology, from Eindhoven University of Technology, Eindhoven, The Netherlands, in 2011 and 2016, respectively.

Since 2016, he has been working as a Mechatronic System Engineer on medical and high-tech systems development at DEMCON Eindhoven, Eindhoven. From 2016 to 2023, he was affiliated with Demcon Macawi Respiratory Systems and, from the beginning in 2024, to Demcon Life Sciences and Health. His main research interests include (hybrid/nonlinear) control, dynamics, and system engineering.

**Nathan van de Wouw** (Fellow, IEEE) received the M.Sc. degree (Hons.) and the Ph.D. degree in mechanical engineering from Eindhoven University of Technology, Eindhoven, The Netherlands, in 1994 and 1999, respectively.

He currently holds a Full Professor Position with the Mechanical Engineering Department, Eindhoven University of Technology. He has been working with Philips Applied Technologies, Eindhoven, in 2000, and Netherlands Organization for Applied Scientific Research, The Hague, The Netherlands, in 2001. From 2006 to 2007, he was a Visiting Professor with the University of California at Santa Barbara, Santa Barbara, CA, USA, the University of Melbourne, Melbourne, NSW, Australia, from 2009 to 2010, and the University of Minnesota, Minnesota, MN, USA, from 2012 to 2013. He has held a (part-time) Full Professor Position with Delft University of Technology, Delft, The Netherlands, from 2015 to 2019. He has also held an Adjunct Full Professor Position with the University of Minnesota from 2014 to 2021. He has published the books *Uniform Output Regulation of Nonlinear Systems: A convergent Dynamics Approach with A.V. Pavlov and H. Nijmeijer* (Birkhauser, 2005) and *Stability and Convergence of Mechanical Systems with Unilateral Constraints with R.I. Leine* (Springer-Verlag, 2008).

Dr. van de Wouw received the IEEE Control Systems Technology Award "for the development and application of variable-gain control techniques for high-performance motion systems" in 2015. He is an IEEE Fellow for his contributions to hybrid, data-based, and networked control.

**Tom Oomen** (Senior Member, IEEE) received the M.Sc. degree (cum laude) and the Ph.D. degree from Eindhoven University of Technology, Eindhoven, The Netherlands, in 2005 and 2010, respectively.

He currently holds a Full Professor Position with the Department of Mechanical Engineering, Eindhoven University of Technology. He is also a part-time Full Professor with Delft University of Technology, Delft, The Netherlands. He held Visiting Positions with KTH, Stockholm, Sweden, and The University of Newcastle, Callaghan, NSW, Australia. His research interests are in the field of data-driven modeling, learning, and control, with applications in precision mechatronics.

Dr. Oomen is a member of Eindhoven Young Academy of Engineering. He was a recipient of the Seventh Grand Nagamori Award, the Corus Young Talent Graduation Award, the IFAC 2019 TC 4.2 Mechatronics Young Research Award, the 2015 IEEE TRANSACTIONS ON CONTROL SYSTEMS TECHNOLOGY Outstanding Paper Award, the 2017 IFAC Mechatronics Best Paper Award, the 2019 IEEJ Journal of Industry Applications Best Paper Award, and a Veni and Vidi Personal Grant. He is currently a Senior Editor of IEEE CONTROL SYSTEMS LETTERS (L-CSS) and an Associate Editor of *IFAC Mechatronics*. He has served on the editorial boards of IEEE CONTROL SYSTEMS LETTERS (L-CSS) and IEEE TRANSACTIONS ON CONTROL SYSTEMS TECHNOLOGY. He has also been the Vice-Chair for IFAC TC 4.2.